Electronic Supplementary Information

Understanding the dopant of hole-transport polymer for efficient inverted perovskite solar cells with high electroluminescence

Qisen Zhou,[a] Junming Qiu,[a] Rongshan Zhuang,[b] Xinyi Mei,[a] Yong Hua,[b*] and Xiaoliang Zhang [a*]

[a] School of Materials Science and Engineering, Beihang University, Beijing 100191, China.
E-mail: xiaoliang.zhang@buaa.edu.cn
[b] Yunnan Key Laboratory for Micro/Nano Materials & Technology, School of Materials and Energy, Yunnan University, Kunming 650091, China.
E-mail: huayong@ynu.edu.cn

Content

Fig. S27. EL emission spectrum of PSCs operated as a LED.

S2. Supplementary Tables

Table S1. Fitted parameters of the TRPL curves of PVK, PTAA/PVK and PTAA+F4TCNQ/PVK samples.

Table S2. Fitted parameters of the fs-TA curves of PVK, PTAA/PVK and PTAA+F4TCNQ/PVK samples.

Table S3. Fitted parameters of the ns-TA curves of PVK, PTAA/PVK and PTAA+F4TCNQ/PVK samples.

Table S4. Summarized photovoltaic performance of the PTAA-based inverted PSCs.

Table S5. Fitted parameters of the TPV curves of PTAA and PTAA+F4TCNQ-based PSCs.

S3. Supplementary References

Experimental Section

Materials: N,N-dimethylformamide (DMF, anhydrous, 99.8%), dimethyl sulfoxide (DMSO, anhydrous, 99.8%), chlorobenzene (CB, anhydrous, 99.8%) were obtained from Sigma-Aldrich. Poly(triarylamine) (PTAA), Formamidinium iodide (FAI), methylammonium bromide (MABr) and bathocuproine (BCP) were purchased from Xi'an Polymer Light Technology Corp. Lead iodide (PbI_2), lead bromide ($PbBr_2$) and 2,3,5,6-tetrafluoro-7,7,8,8-tetracyanoquinodimethane (F4TCNQ) were purchased from TCI. All chemicals were used without any further purification.

Solar Cell Fabrication: The ITO glass substrate was ultrasonically cleaned with acetone, deionized water and ethanol sequentially and dried by nitrogen flow. The cleaned ITO substrate was further treated with UV-ozone and then transferred to the glovebox. The PTAA film was deposited on the ITO substrate by spin coating at 5000 rpm and then annealed at 100 ℃ for 10 min. For the PTAA+F4TCNQ sample, the F4TCNQ stock solution was prepared by dissolving F4TCNQ in chlorobenzene, and then the prepared F4TCNQ stock solution was added into the PTAA solution (5 mg/ml in toluene) with a weight ratio of 1%. To prepare the perovskite precursor solution, 95% (volume ratio) solution of PbI_2 (1.1 M), $PbBr_2$ (0.2 M), FAI (1 M), and MABr (0.2 M) in a mixed solvent of DMF: DMSO = 4:1 (volume ratio) and 5% CsI (1.5 M) solution in DMSO were mixed together. The perovskite films were prepared on the PTAA or PTAA+F4TCNQ layer by spin coating at 1000 rpm for 10 s and 5000 rpm for 30 s, and 150 mL of chlorobenzene used as an antisolvent was dropped on the spinning samples at 15 s before the end. Then, the perovskite layer was annealed at 100 ℃ for 45 min. The phenylethyl ammonium iodide solution was spin-coated on the surface of the perovskite layer at 4000 rpm for 30 s and subsequently annealed at 100 ℃ for 15 min. Then, the PCBM film was deposited on the perovskite layer by spin coating at 2000 rpm with a solution (20 mg/ml PCBM in CB). The BCP film was prepared on the PCBM layer by spin coating at 5000 rpm with a solution (0.5 mg/ml BCP in ethanol). Finally, the 100 nm Ag electrode was thermal evaporated on the BCP layer to finish PSCs.

Material Characterization: The Raman spectrometer (Renishaw inVia) was used to measure the Raman spectra. The scanning electron microscope (JEOL-7500) was used to record the Scanning electron microscopy (SEM) images with an accelerating voltage of 3 kV. The Nicolet 6700 Fourier Transform Infrared Spectrometer was used to measure the Fourier transform infrared (FTIR) spectrum. The Bruker AVANCE III 600M NMR spectrometer was used to conduct the ^1H nuclear magnetic resonance (NMR) measurements. The Ocean Optical fluorophotometer was used to measure the steady-state photoluminescence (PL) spectrum. The FLS980 spectrometer was used to record the time-resolved PL (TRPL) decay with an excitation wavelength of 485 nm.

X-ray photoelectron spectroscopy (XPS) was recorded using *X*-ray photoelectron spectrometer (Thermo Scientific Escalab 250Xi US) with a micro-focus monochromatic Al Kα *X*-ray source. Femtosecond transient absorption (fs-TA) measurements were carried out using a multipass amplified Ti: sapphire laser (800 nm laser pulses; pulse width of ~120 fs with a repetition rate of 2 kHz; the detection time delay is in the range of 8.5 ns in conjunction with Helios spectrometers). Excitation pump pulses were generated after passing through a fraction of the 800 nm beam into a spectrally tunable (240-2600 nm) optical parametric amplifier (Newport Spectra Physics). Nanosecond transient absorption (ns-TA) measurements were performed using a transient absorption spectrometer (LP980).

Device Characterization: The *J-V* curve of unencapsulated PSCs was recorded by a digital source meter (Keithley 2400) in the ambient atmosphere. To study the hysteresis, both forward (from J_{sc} to V_{oc}) and the reverse (from V_{oc} to J_{sc}) voltage scanning directions were performed with a voltage scanning speed of 100 mV/s during the *J-V* measurement. The AAA class solar simulator (Enli SS-F5-3A) was used to supply the AM1.5G 100 mW/cm^2 illumination and the light intensity was calibrated using a certified silicon reference cell (Fraunhofer ISE). The black metallic mask (0.06 cm^2) was used to define the working area of PSCs. The IPCE spectrum was recorded using an Enli Technology QE-R system including a Czerny-Turner monochromator (QE-M110), a xenon lamp (QE-LD), a light intensity detection system (QE-M1) and an optical imaging system. The Zahner Zennium CIMPS-pro electrochemical workstation was used to record the transient photovoltage (TPV) decay under 100 mW/cm^2 illumination supplied by the white light source (Zahner, LSW-2). The related tests operating PSC as LED was measured using the Enlitech measurement system (LQ-100).

Computational Method: The Vienna *Ab initio* Simulation Package (VASP) was used to perform first-principles calculations.[1, 2] The generalized gradient approximation (GGA) in Perdew-Burke-Ernzerhof (PBE) was used to compute exchange and correlation energies.[3, 4] Grimme's DFT-D3 was used for dispersion correction.[5] The cubic-phased 2 × 2 × 2 supercells were used to build the surface slab model with 20 Å vacuum layer. The cutoff energy for the plane wave expansion was set as 400 eV. The Monkhorst-Pack k-point mesh of (2 × 2 × 1) was adopted. Then the atom positions were relaxed until the energy convergence was less than 1.0 × 10^{-5} eV and the force was less than 0.05 eV/Å. The binding energy (E_b) is calculated from the equation of $E_b = E_{total} - E_{PVK} - E_{molecule}$, where E_{total} is the total energy of the slap after the perovskite-molecule interactions, E_{PVK} and $E_{molecule}$ are the energy of the perovskite and the molecule before interactions, respectively.

S1. Supplementary Figures

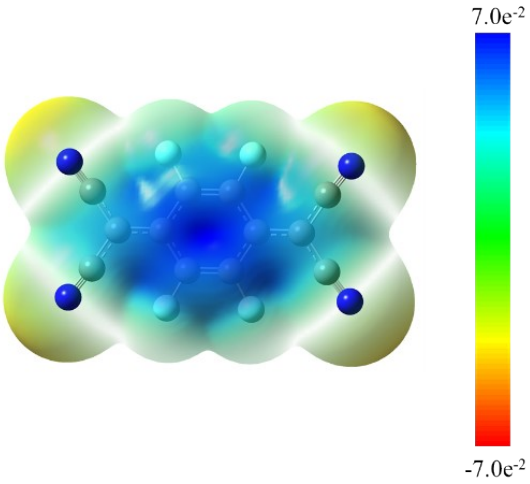

Fig. S1. The electrostatic potential distribution of the F4TCNQ molecule.

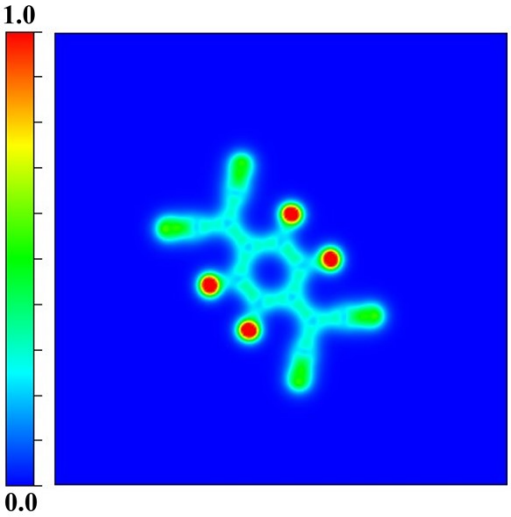

Fig. S2. The charge density distribution of the F4TCNQ molecule.

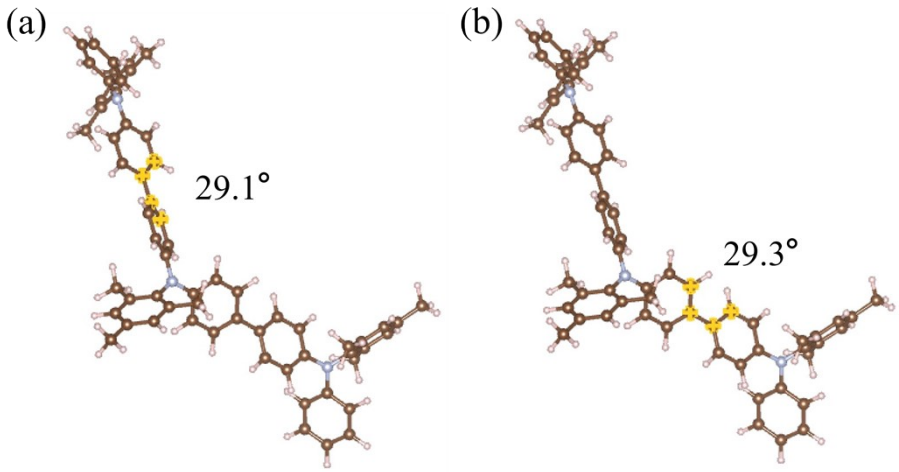

Fig. S3. The optimized structure of the trimer of PTAA. The two dihedral angle values in the trimer of PTAA are almost similar that are (a) 29.1° and (b) 29.3°, respectively.

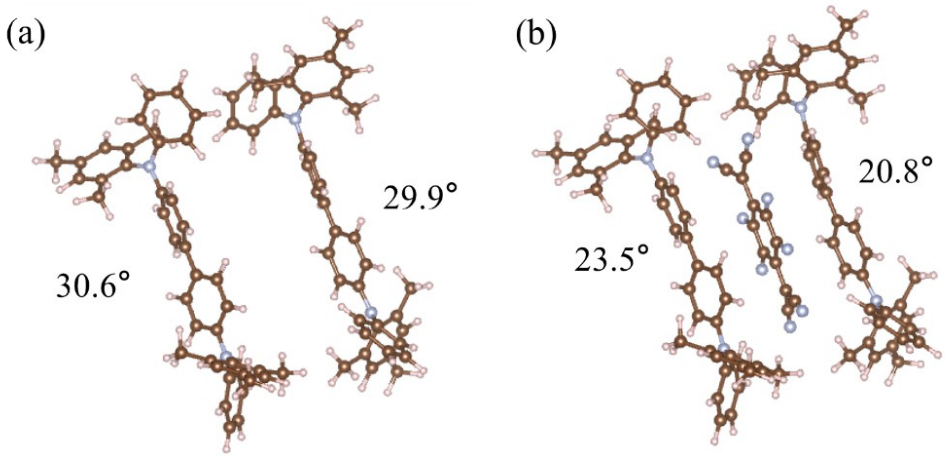

Fig. S4. The optimized structure of (a) d-PTAA/d-PTAA and (b) d-PTAA/F4TCNQ/d-PTAA systems. The dihedral angle of d-PTAA is decreased after the introduction of F4TCNQ molecules.

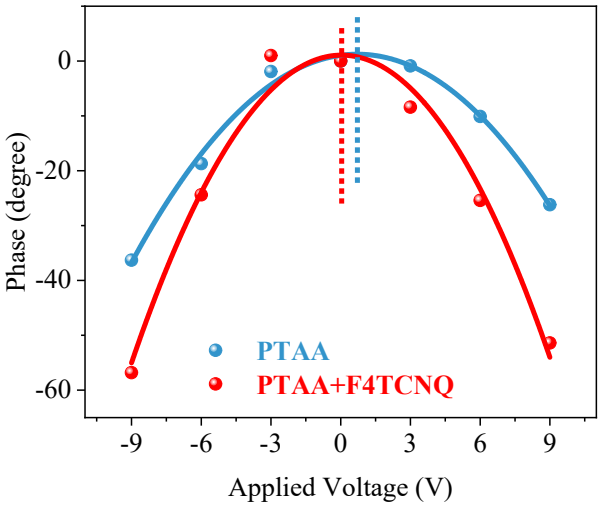

Fig. S5. Plots of the phase as a function of the applied voltage bias. The primary PTAA layer is slightly positively charged as the symmetry axis of the fitted parabola is positive. After introducing F4TCNQ into the PTAA layer, the symmetry axis of the fitted parabola shifted to the negative direction, which may be attributed to the high electron affinity of F4TCNQ molecules that could lead to charge transfer from PTAA to F4TCNQ and the ionization of F4TCNQ by environmental factors.

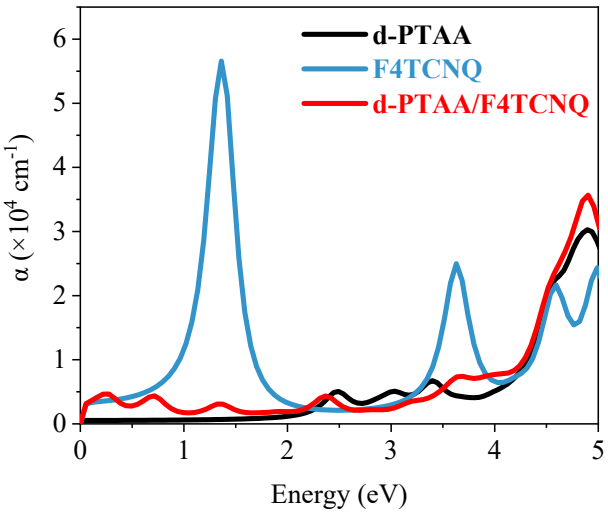

Fig. S6. The calculated absorption spectra of d-PTAA, F4TCNQ and d-PTAA/F4TCNQ systems. The results show that the new band gap could be observed at the position less than 1 eV, which may be attributed to the charge transfer between the d-PTAA and F4TCNQ.

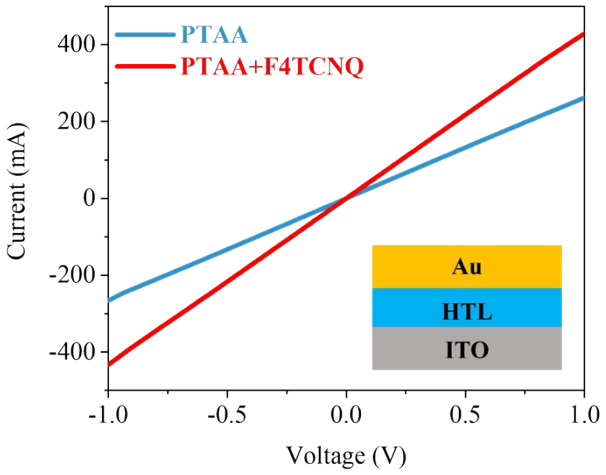

Fig. S7. *I-V* curves of the ITO/PTAA/Au and ITO/PTAA+F4TCNQ/Au devices.

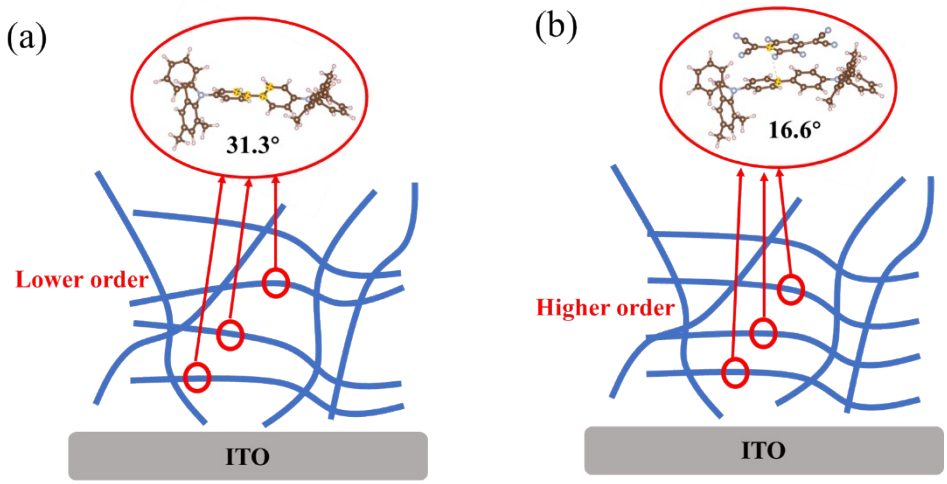

Fig. S8. Proposed schematic diagrams of the microstructure and molecular arrangement of (a) PTAA and (b) PTAA+F4TCNQ layer.

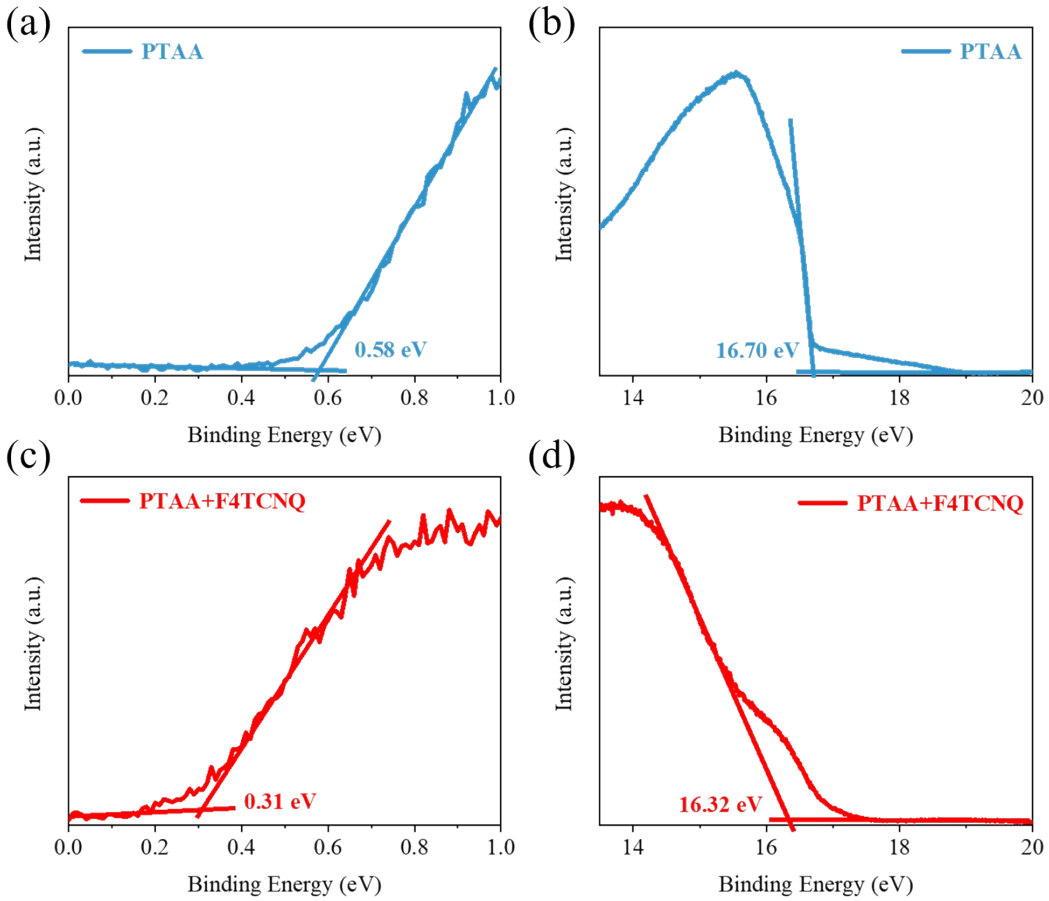

Fig. S9. (a, c) Near Fermi edge region and (b, d) cut-off energy region of the UPS spectra of PTAA and PTAA+F4TCNQ layer, respectively.

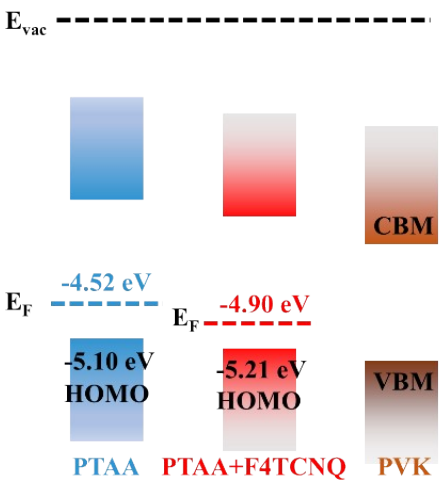

Fig. S10. The energy level diagram of PTAA, PTAA+F4TCNQ and perovskite layers.

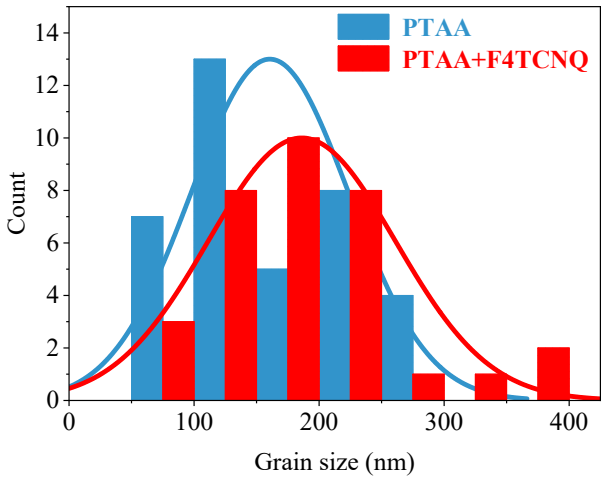

Fig. S11. Grain size distributions of perovskite films deposited on the PTAA and PTAA+F4TCNQ layers.

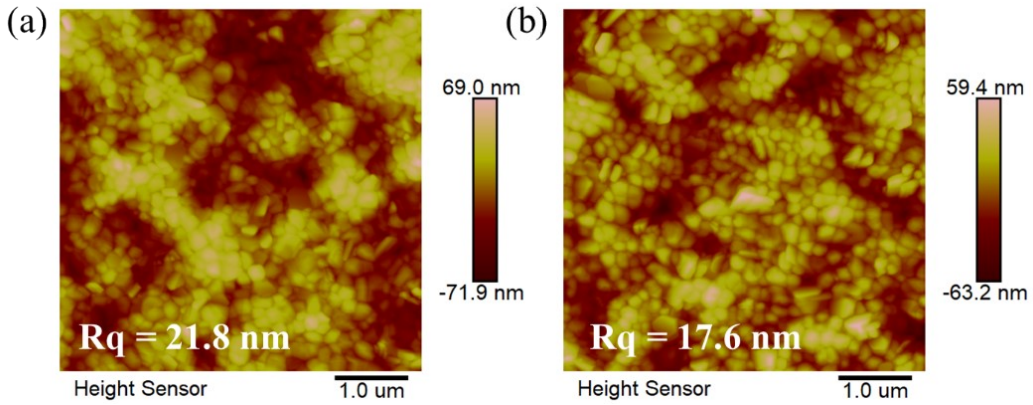

Fig. S12. AFM images of perovskite films deposited on the (a) PTAA and (b) PTAA+F4TCNQ layers.

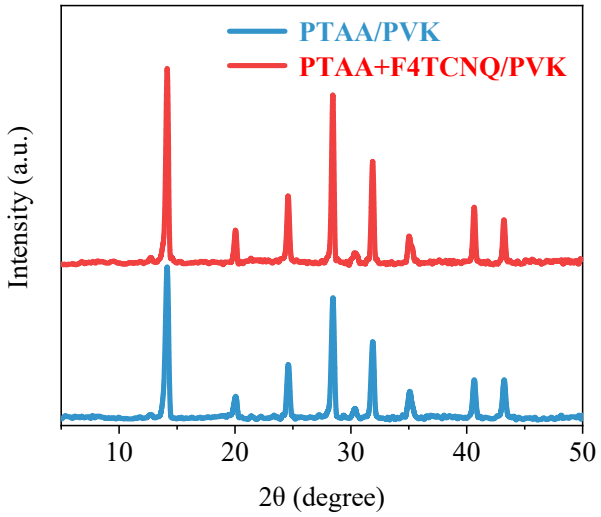

Fig. S13. XRD patterns of PTAA/PVK and PTAA+F4TCNQ/PVK samples.

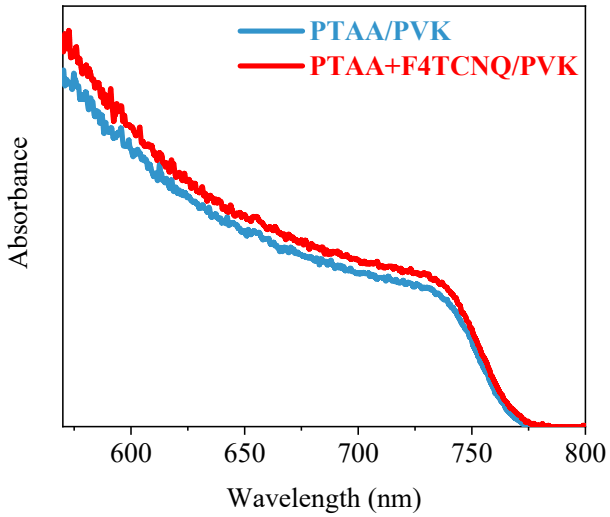

Fig. S14. Light absorption spectra of PTAA/PVK and PTAA+F4TCNQ/PVK samples.

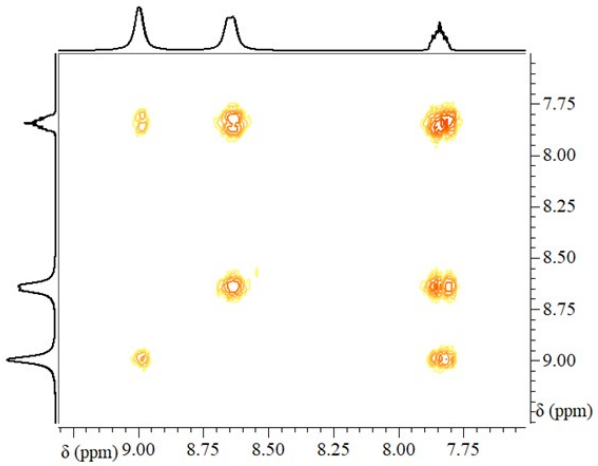

Fig. S15. ^{1}H-^{1}H COSY spectroscopy of mixed F4TCNQ and FAI.

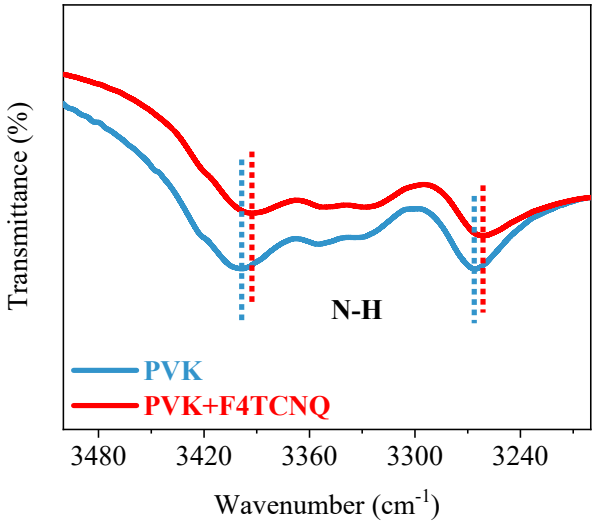

Fig. S16. The FTIR spectra of the perovskite films without and with doped with F4TCNQ.

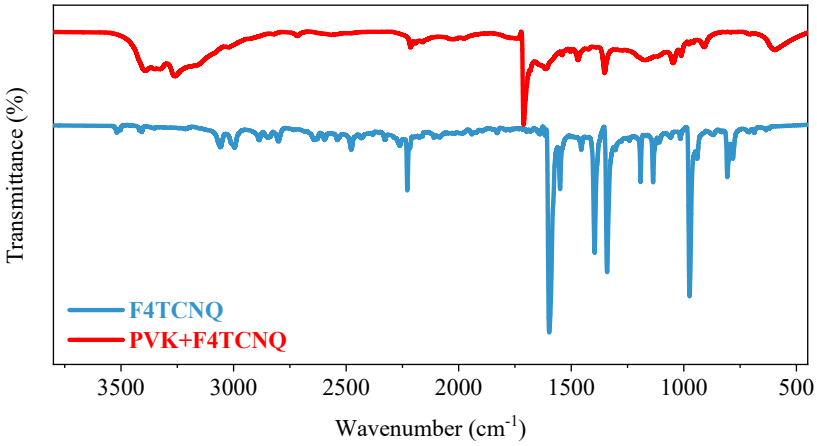

Fig. S17. Full FTIR spectra of F4TCNQ and the perovskites doped with F4TCNQ.

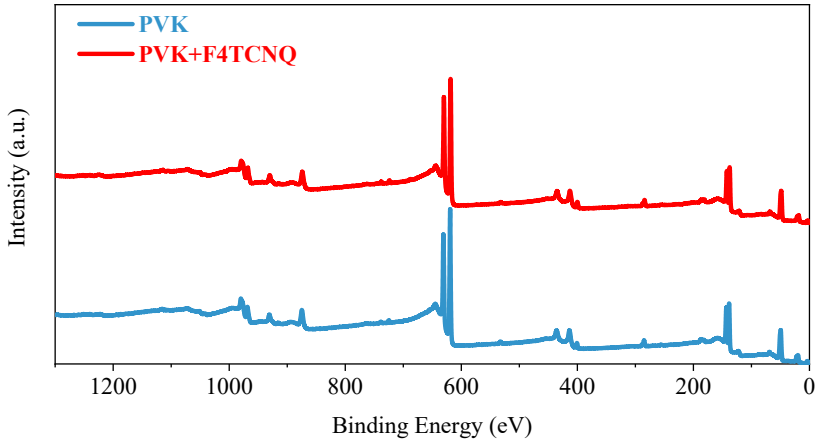

Fig. S18. Overview XPS spectra of primary perovskites and the perovskites doped with F4TCNQ.

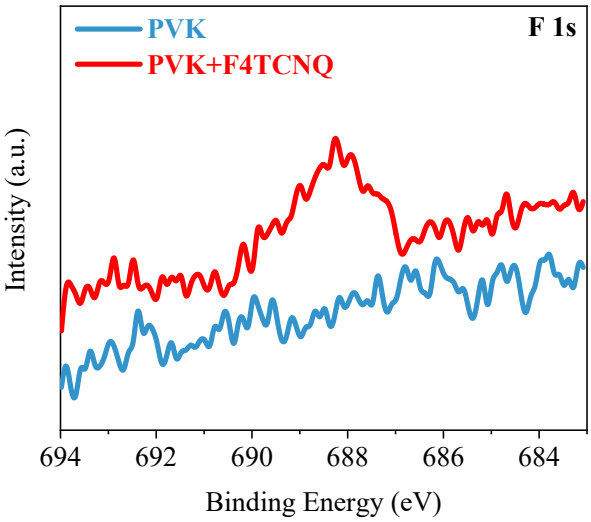

Fig. S19. Core-level XPS spectra of F 1s of primary perovskites and the perovskites doped with F4TCNQ.

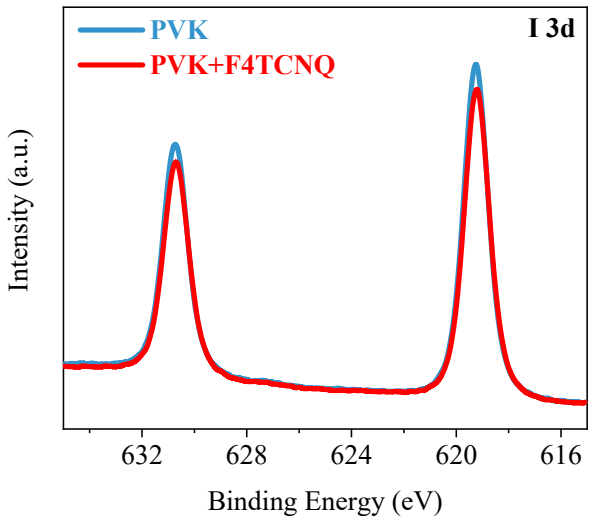

Fig. S20. Core-level XPS spectra of I 3d of primary perovskites and the perovskites doped with F4TCNQ.

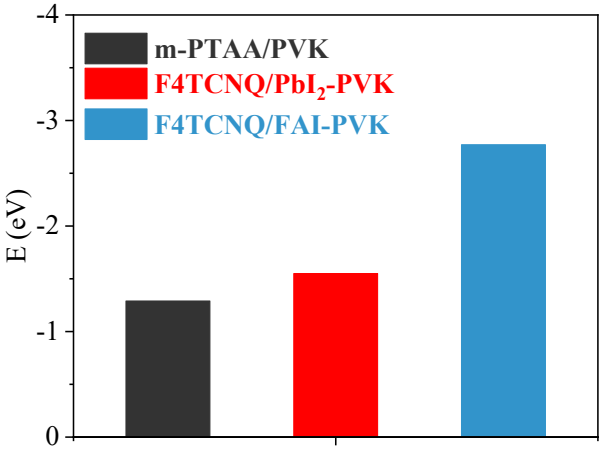

Fig. S21. The calculated binding energies of m-PTAA/PVK, F4TCNQ/PbI_2-PVK and F4TCNQ/FAI-PVK systems.

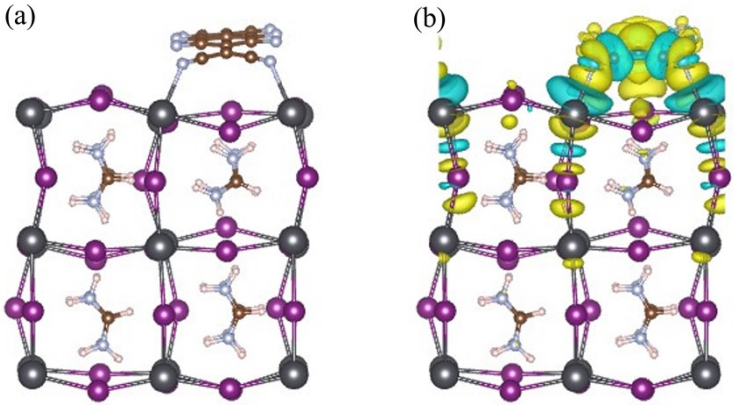

Fig. S22. The side view of (a) the F4TCNQ/PbI_2-PVK system and (b) corresponding charge density differences.

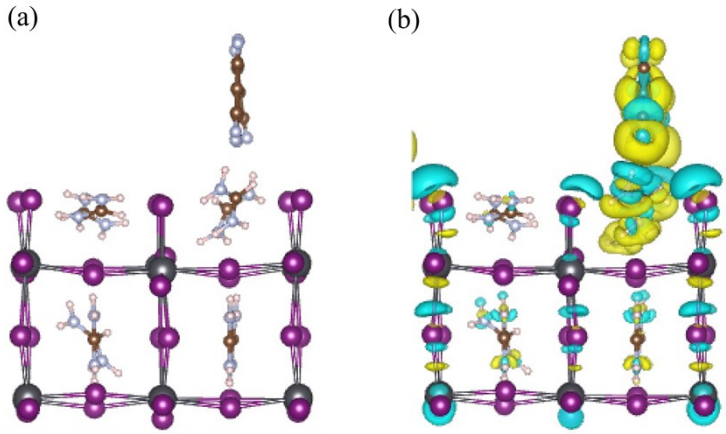

Fig. S23. The side view of (a) the F4TCNQ/FAI-PVK system and (b) corresponding charge density differences.

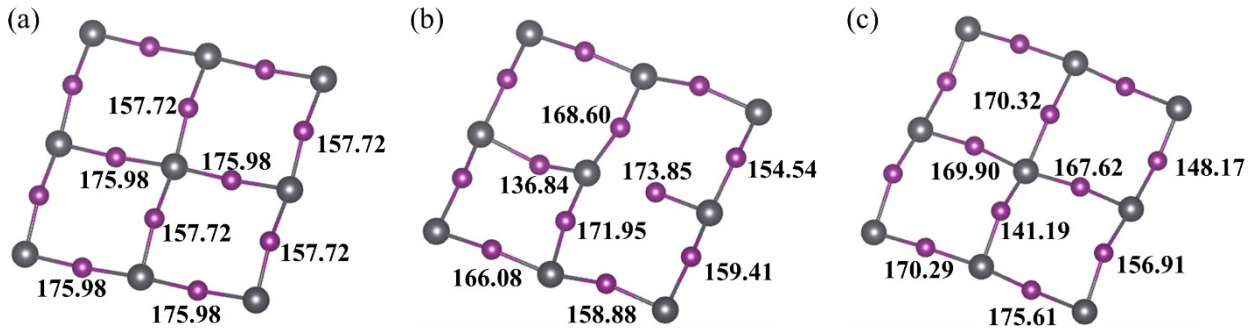

Fig. S24. The Pb-I-Pb bond angles of perovskite surface of (a) PVK, (b) m-PTAA/PVK and (c) F4TCNQ/PbI_2-PVK systems. The unit of angle values in the figure is °. The average value of the Pb-I-Pb bond angle on the perovskite surface of PVK, m-PTAA/PVK, and F4TCNQ/PbI_2-PVK systems was calculated to be 166.85°, 161.27° and 162.50°. Moreover, the maximum and minimum values of the Pb-I-Pb bond angle of the perovskite surface of m-PTAA/PVK systems were determined to be 173.85° and 136.84°, and the maximum and minimum values of the Pb-I-Pb bond angle of perovskite surface of F4TCNQ/PbI_2-PVK systems were determined to be 175.61° and 141.19°, respectively. Obviously, the average, maximum and minimum values of the Pb-I-Pb bonding angle of the perovskite surface of the F4TCNQ/PbI_2-PVK system are closer to the perfect perovskite cell values than those of m-PTAA/PVK system. Therefore, it can be concluded that compared with the interaction with m-PTAA, the interaction between perovskite and F4TCNQ makes perovskite have a more perfect crystal structure, which strongly proves that the introduction of F4TCNQ is beneficial to the crystallization and growth of perovskite films.

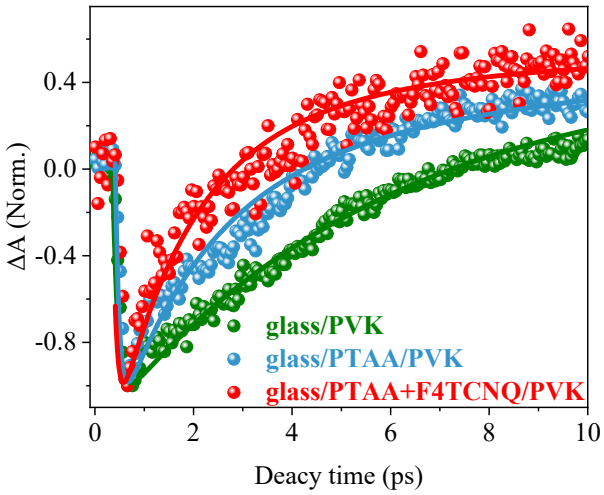

Fig. S25. The fs-TA spectra of glass/PVK, glass/PTAA/PVK and glass/PTAA+F4TCNQ/PVK samples.

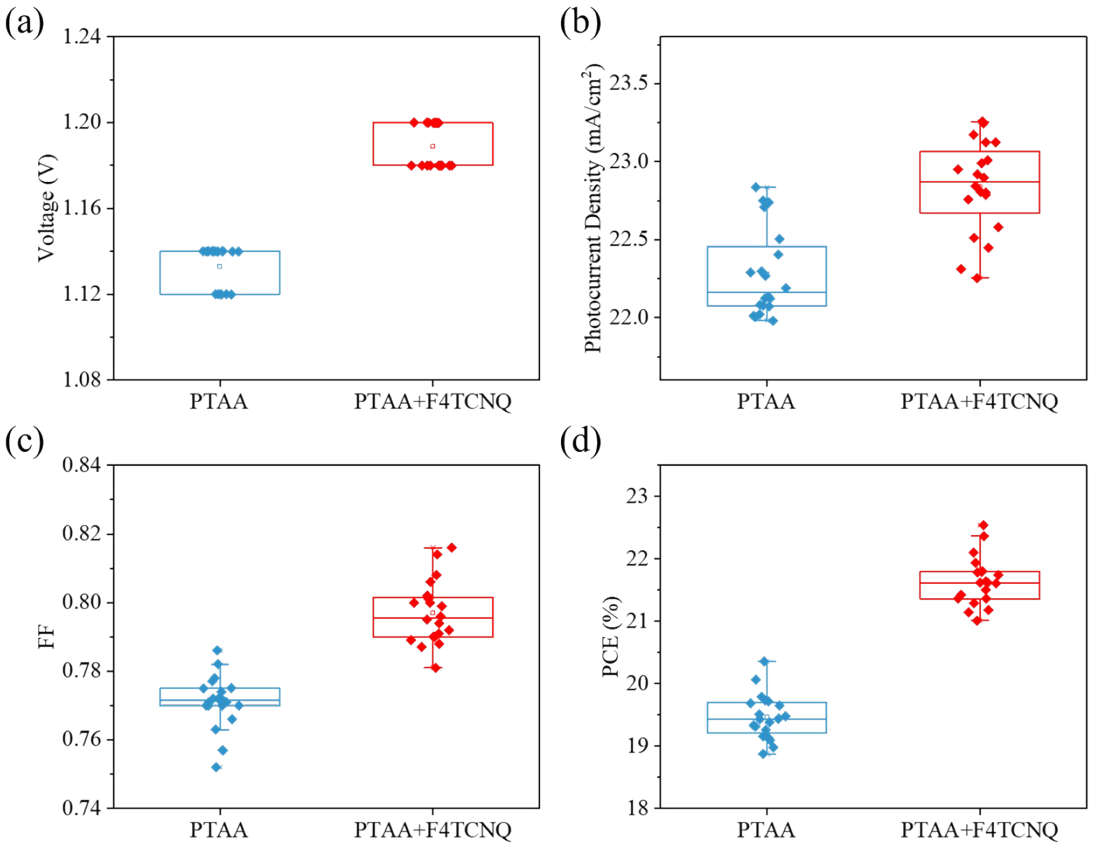

Fig. S26. Photovoltaic parameter statistics of (a) V_{oc}, (b) J_{sc}, (c) FF and (d) PCE of PTAA and PTAA+F4TCNQ-based PSCs. 20 devices fabricated from different branches were applied for statistics.

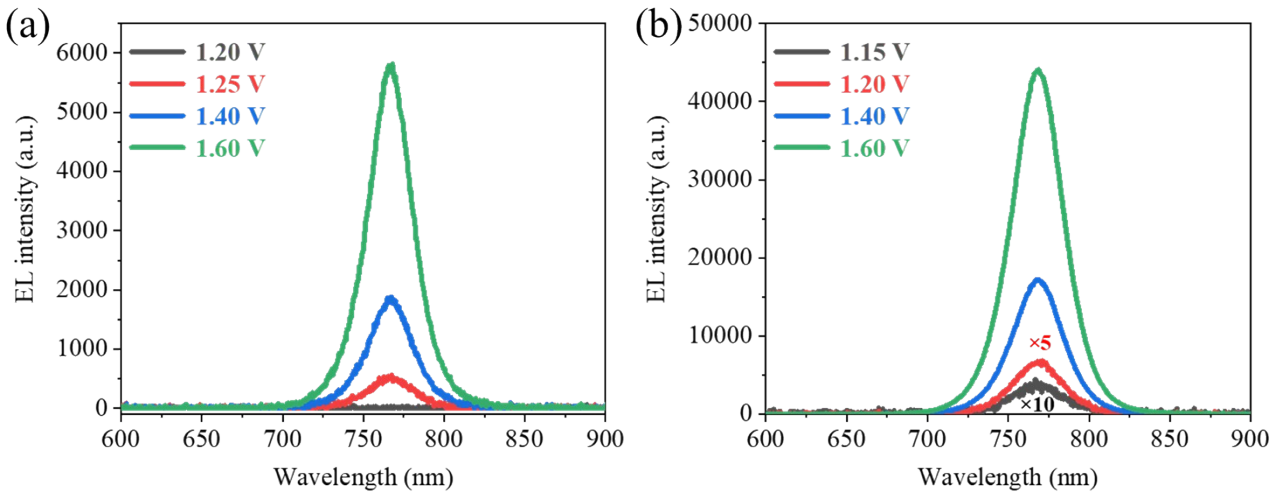

Fig. S27. EL emission spectra of (a) PTAA and (b) PTAA+F4TCNQ-based PSCs operated as LED devices under different voltage bias.

S2. Supplementary Tables

Table S1. Fitted parameters of the TRPL curves of PVK, PTAA/PVK and PTAA+F4TCNQ/PVK samples.

Sample	A	τ_1 (ns)	B	τ_2 (ns)	τ_{ave} (ns)
PVK	46.05	402.43	178.40	1505.12	1433.93
PTAA/PVK	228.12	84.50	151.95	354.85	283.65
PTAA+F4TCNQ/PVK	505.17	36.82	18.78	291.51	94.74

The PL decay curve was fitted using the following equation,[6]

$$I(t) = A \cdot exp\left(-\frac{t}{\tau_1}\right) + B \cdot exp\left(-\frac{t}{\tau_2}\right) + C \quad \text{(Eq. 1)}$$

where A, B, and C are constants, t is PL decay time, τ_1 and τ_2 are fitted lifetimes.

The average lifetime,τ_{ave}, was calculated using the following equation,

$$\tau_{ave} = \frac{A{\tau_1}^2 + B{\tau_2}^2}{A\tau_1 + B\tau_2} \quad \text{(Eq. 2)}$$

Table S2. Fitted parameters of the fs-TA curves of PVK, PTAA/PVK and PTAA+F4TCNQ/PVK samples.

Sample	A	τ_1 (ps)	B	τ_2 (ps)	τ_{ave} (ps)
glass/PVK	-0.78	5.68	-0.80	-5.68	5.68
glass/PTAA/PVK	-0.74	3.69	-0.86	3.69	3.69
glass/PTAA+F4TCNQ/PVK	-9.40	0.21	-1.43	3.67	2.72

The decay was fitted using the following equation,

$$I(t) = A \cdot exp\left(-\frac{t}{\tau_1}\right) + B \cdot exp\left(-\frac{t}{\tau_2}\right) + C \quad \text{(Eq. 3)}$$

where A, B, and C are constants, t is decay time, τ_1 and τ_2 are fitted lifetimes.

The average lifetime, τ_{ave}, was calculated using the following equation,

$$\tau_{ave} = \frac{A{\tau_1}^2 + B{\tau_2}^2}{A\tau_1 + B\tau_2} \quad \text{(Eq. 4)}$$

Table S3. Fitted parameters of the ns-TA curves of PVK, PTAA/PVK and PTAA+F4TCNQ/PVK samples.

Sample	A	τ_1 (ns)	B	τ_2 (ns)	τ_{ave} (ns)
glass/PVK	-0.02	393.45	-0.01	4602.30	3597.47
glass/PTAA/PVK	-0.05	664.45	-0.02	6365.08	5049.35
glass/PTAA+F4TCNQ/PVK	-0.06	859.85	-0.02	7651.08	6081.15

The decay was fitted using the following equation,

$$I(t) = A \cdot exp\left(-\frac{t}{\tau_1}\right) + B \cdot exp\left(-\frac{t}{\tau_2}\right) + C \quad \text{(Eq. 5)}$$

where A, B, and C are constants, t is decay time, τ_1 and τ_2 are fitted lifetimes.

The average lifetime, τ_{ave}, was calculated using the following equation,

$$\tau_{ave} = \frac{A{\tau_1}^2 + B{\tau_2}^2}{A\tau_1 + B\tau_2} \quad \text{(Eq. 6)}$$

Table S4. Summarized photovoltaic performance of the PTAA-based inverted PSCs.

Device structure	V_{oc} (V)	J_{sc} (mA/cm^2)	FF	PCE (%)	Ref.
ITO/PTAA/$(FA_{0.95}PbI_{2.95})_{0.85}(MAPbBr_3)_{0.15}$/SSG-G/PCBM/C60/BCP/Cu	1.21	22.50	0.790	21.51	7
ITO/PTAA/$Cs_{0.05}(FA_{0.85}MA_{0.15})_{0.95}Pb(I_{0.85}Br_{0.15})_3$/ PCBM/ZrL3:bis-C60/Ag	1.20	22.58	0.8128	22.02	8
ITO/PTAA/PMMA/$Cs_{0.05}(FA_{0.85}MA_{0.85})_{0.95}Pb(I_{0.85}Br_{0.15})_3$ /C60/BCP/Ag	1.12	23.06	0.80	20.75	9
ITO/PTAA/$Cs_{0.05}(FA_{0.85}MA_{0.15})_{0.95}Pb(I_{0.85}Br_{0.15})_3$/$FcTc_2$ /C60/BCP/Ag	1.176	22.76	0.8137	21.8	10
ITO/NiOx/PTAA/ /$Cs_{0.05}(FA_{0.90}MA_{0.10})_{0.95}Pb(I_{0.90}Br_{0.10})_3$/PCBM/BCP/Ag	1.13	24.3	0.809	22.1	11
ITO/PTAA/ASMs/$(Cs_{0.05}FA_{0.81}MA_{0.14})Pb(I_{0.86}Br_{0.14})_3$ /PCBM/C60/LiF/Cu	1.11	21.95	0.81	19.7	12
ITO/PTAA/$Cs_{0.05}FA_{0.83}MA_{0.12}PbI_{2.62}Br_{0.38}$ /PEAI/PCBM/ZnO/Ag	1.18	22.75	0.793	21.31	13
ITO/PTAA/LAIs/ $(CsPbI_3)_{0.05}(FA_{0.85}MA_{0.15}Pb(I_{0.85}Br_{0.15})_3)_{0.95}$/PCBM/BCP/Ag	1.21	22.59	0.8163	22.31	14
ITO/PTAA/PFN-P2/ $(Cs_{0.05}(MA_{0.17}FA_{0.83})_{0.95})Pb(I_{0.83}Br_{0.17})_3$/C60/BCP/Cu	1.158	22.54	0.8193	21.39	15
ITO/PTAA+F4TCNQ/ $Cs_{0.05}(FA_{0.83}MA_{0.17})_{0.95}Pb(I_{0.83}Br_{0.17})_3$/PCBM/BCP/Ag	1.20	23.2	0.808	22.5	This work

Table S5. Fitted parameters of the TPV curves of PTAA and PTAA+F4TCNQ-based PSCs.

Device	A	τ_1 (ms)	B	τ_2 (ms)	τ_{ave} (ms)
PTAA	0.42	0.13	0.55	0.87	0.79
PTAA+F4TCNQ	0.41	0.14	0.60	2.03	1.94

The V_{oc} decay was fitted using the following equation,[16]

$$V_{OC} = A \cdot exp\left(-\frac{t}{\tau_1}\right) + B \cdot exp\left(-\frac{t}{\tau_2}\right) + C \quad \text{(Eq. 7)}$$

where A, B, and C are constants, t is V_{oc} decay time, τ_1 and τ_2 are fitted lifetimes.

The average lifetime, $\tau_{ave,}$ was calculated using the following equation,

$$\tau_{ave} = \frac{A{\tau_1}^2 + B{\tau_2}^2}{A\tau_1 + B\tau_2} \quad \text{(Eq. 8)}$$

S3. Supplementary References

1 G. Kresse and J. Furthmüller, *Comput. Mater. Sci.*, 1996, **6**, 15-50.
2 Kresse and Hafner, *Phys. Rev. B*, 1993, **47**, 558-561.
3 S. Grimme, J Comput Chem, 2006, **27**, 1787-1799.
4 M. C. Payne, M. P. Teter, D. C. Allan, T. A. Arias and J. D. Joannopoulos, *Rev. Mod. Phys.*, 1992, **64**, 1045-1097.
5 S. Grimme, J. Antony, S. Ehrlich and H. Krieg, *J. Chem. Phys.*, 2010, 132, 154104.
6 J. Liu, Q. Zhou, N. K. Thein, L. Tian, D. Jia, E. M. J. Johansson and X. Zhang, *J. Mater. Chem. A*, 2019, **7**, 13777-13786.
7 D. Y. Luo, W. Q. Yang, Z. P. Wang, A. Sadhanala, Q. Hu, R. Su, R. Shivanna, G. F. Trindade, J. F. Watts, Z. J. Xu, T. H. Liu, K. Chen, F. J. Ye, P. Wu, L. C. Zhao, J. Wu, Y. G. Tu, Y. F. Zhang, X. Y. Yang, W. Zhang, R. H. Friend, Q. H. Gong, H. J. Snaith and R. Zhu, *Science*, 2018, **360**, 1442-1446.
8 S. Wu, Z. Li, M. Q. Li, Y. Diao, F. Lin, T. Liu, J. Zhang, P. Tieu, W. Gao, F. Qi, X. Pan, Z. Xu, Z. Zhu and A. K. Jen, *Nat. Nanotechnol.*, 2020, **15**, 934-940.
9 X. Liu, Y. Cheng, C. Liu, T. Zhang, N. Zhang, S. Zhang, J. Chen, Q. Xu, J. Ouyang and H. Gong, *Energy Environ. Sci.*, 2019, **12**, 1622-1633.
10 Z. Li, B. Li, X. Wu, S. A. Sheppard, S. Zhang, D. Gao, N. J. Long and Z. Zhu, *Science*, 2022, **376**, 416-420.
11 B. Niu, H. Wu, J. Yin, B. Wang, G. Wu, X. Kong, B. Yan, J. Yao, C.-Z. Li and H. Chen, *ACS Energy Lett.*, 2021, **6**, 3443-3449.
12 W. Lv, Z. Hu, W. Qiu, D. Yan, M. Li, A. Mei, L. Xu and R. Chen, Adv Sci (Weinh), 2022, 9, e2202028.
13 C. Zhang, S. Wu, L. Tao, G. M. Arumugam, C. Liu, Z. Wang, S. Zhu, Y. Yang, J. Lin, X. Liu, R. E. I. Schropp and Y. Mai, *Adv. Energy Mater.*, 2020, **10**, 2002004.
14 S. Wu, J. Zhang, Z. Li, D. Liu, M. Qin, S. H. Cheung, X. Lu, D. Lei, S. K. So, Z. Zhu and A. K. Y. Jen, *Joule*, 2020, **4**, 1248-1262.
15 P. Caprioglio, D. S. Cruz, S. Caicedo-Dávila, F. Zu, A. A. Sutanto, F. Peña-Camargo, L. Kegelmann, D. Meggiolaro, L. Gregori, C. M. Wolff, B. Stiller, L. Perdigón-Toro, H. Köbler, B. Li, E. Gutierrez-Partida, I. Lauermann, A. Abate, N. Koch, F. De Angelis, B. Rech, G. Grancini, D. Abou-Ras, M. K. Nazeeruddin, M. Stolterfoht, S. Albrecht, M. Antonietti and D. Neher, Energy & Environmental *Science*, 2021, **14**, 4508-4522.
16 X. Zhang, J. Zhang, D. Phuyal, J. Du, L. Tian, V. A. Öberg, M. B. Johansson, U. B. Cappel, O. Karis, J. Liu, H. Rensmo, G. Boschloo and E. M. J. Johansson, *Adv. Energy Mater.*, 2018, **8**, 1702049.